







Effects of hydrogen concentration in ablator material on stimulated Raman scattering, two-plasmon decay, and hot electrons for direct-drive inertial confinement fusion

K. Kawasaki ^{1,*}, G. Cristoforetti,² T. Idesaka,¹ Y. Hironaka,¹ D. Tanaka,¹ D. Batani,³ S. Fujioka ¹, L. A. Gizzi,² M. Hata,⁴ T. Johzaki ⁵, K. Katagiri ⁶, R. Kodama,^{1,6} S. Matsuo,¹ H. Nagatomo,¹ Ph. Nicolai,³ N. Ozaki ^{1,6}, Y. Sentoku,¹ R. Takizawa,¹ A. Yogo,¹ H. Yamada,⁷ and K. Shigemori ¹

¹*Institute of Laser Engineering, Osaka University, 2-6 Yamadaoka, Suita, Osaka 565-0871, Japan*

²*Intense Laser Irradiation Laboratory, INO-CNR, 56124 Pisa, Italy*

³*Centre Lasers Intenses et Applications, CELIA, University Bordeaux CEA-CNRS, UMR 5107, F-33405 Talence, France*

⁴*National Institute for Fusion Science, 332-6 Oroshicho, Toki, Gifu 509-5202, Japan*

⁵*Graduate School of Engineering, Hiroshima University, 1-4-1 Kagamiyama, Higashi-Hiroshima, Hiroshima 739-8527, Japan*

⁶*Graduate School of Engineering, Osaka University, 2-6 Yamadaoka, Suita, Osaka 565-0871, Japan*

⁷*Diamond Material Team, Advanced Power Electronics Research Center, National Institute of Advanced Industrial Science and Technology, 1-8-31 Midorigaoka, Ikeda, Osaka 563-0026, Japan*



(Received 6 March 2023; accepted 12 July 2023; published 25 July 2023)

Laser plasma instabilities, such as stimulated Raman scattering (SRS) and two-plasmon decay (TPD), are basic phenomena in intense laser science and applications. In direct-drive inertial confinement fusion (ICF) where a fuel capsule is imploded by high-power lasers, SRS and TPD are generally problematic because hot electrons (HEs) generated by SRS and TPD cause fuel preheating, whereas HEs with acceptable energy are expected to contribute to ablation pressure enhancement. In all cases, it is necessary to clarify the occurrence of SRS, TPD, and subsequent HE generation. The ablator of a fuel capsule in direct-drive ICF typically consists of carbon with a variable amount of hydrogen (H). We investigated the H effects in the ablator on SRS, TPD, and HEs under direct-drive ICF conditions at the GEKKO laser facility in planer geometry. The experimental results showed an increase in SRS, TPD, and HEs when H was present in the ablator. The analysis indicated that the variations in plasma inhomogeneity and plasma temperature obtained by H addition were insufficient to explain the observed results. Thus, the enhancement is mainly attributed to the high ion acoustic wave damping driven by the H ions into the plasmas, suggesting that Langmuir decay instability caused SRS saturation, whereas other mechanisms, such as cavitation, could overwhelm the TPD saturation. These results suggest that a suitable choice of H concentration in the ablator is critical for mitigating and controlling the extent of SRS, TPD, and HEs to achieve robust and efficient implosion in direct-drive ICF.

DOI: [10.1103/PhysRevResearch.5.033051](https://doi.org/10.1103/PhysRevResearch.5.033051)

I. INTRODUCTION

In direct-drive inertial confinement fusion (ICF), a fuel capsule of a spherical ablator containing cryogenic deuterium and tritium fuel is typically irradiated by an intense laser pulse of 10^{14} to 10^{15} W/cm² [1–3]. Under such conditions, parametric instabilities such as stimulated Raman scattering (SRS) and two-plasmon decay (TPD) are considerable, and the generation of hot electrons (HEs) is generally problematic because they penetrate through the ablator, preheat the fuel, and deteriorate the implosion of the capsule [4]. Conversely, in advanced ICF schemes such as shock ignition [5], HEs with acceptable energy (<100 keV) can also have beneficial

effects on the implosion performance because they can be absorbed inside the ablator and result in an enhanced ablation pressure [6–8]. In all ICF schemes, a deep understanding of HE generation is crucial for mitigating and controlling its effects on capsule compression. HEs are typically produced by Langmuir waves (LWs) driven by SRS and TPD, where laser light decays into an electromagnetic wave (EMW) and a daughter LW and into two daughter LWs, respectively [9,10]. The plasma composition is an important factor that determines the extent of SRS and TPD [11–13]. In ICF, the ablator should have a low atomic number (*Z*) to avoid unacceptable radiation preheating and typically consists of carbon (C) with different hydrogen (H) concentrations: polycrystalline diamond (0 to ~10 at. %) [14–17], diamondlike carbon (~10 to ~50 at. %) [18,19], and hydrocarbons (>~50 at. %) [20]. Therefore, it is important to understand the effects of H concentration in the ablator on SRS and TPD.

In conditions typical for indirect-drive ICF, where the internal surface of the hohlraum consisting of high-*Z* material is irradiated to produce x rays driving the implosion [2], an increase in SRS with increasing H concentration has

*u710983e@ecs.osaka-u.ac.jp

Published by the American Physical Society under the terms of the [Creative Commons Attribution 4.0 International](https://creativecommons.org/licenses/by/4.0/) license. Further distribution of this work must maintain attribution to the author(s) and the published article's title, journal citation, and DOI.

been clearly demonstrated [21–24]. These results suggest that, during laser interaction with homogeneous high-Z plasmas, Langmuir decay instability (LDI) is a dominant saturation mechanism of SRS through the decay of the SRS LW into an ion acoustic wave (IAW) and secondary LW because the LDI threshold increases with the IAW damping rate through the H concentration [21–24]. However, in direct-drive ICF, plasmas consist of low-Z ions and are spatially inhomogeneous. Under these conditions, the growth of laser plasma instabilities is ruled by the limited resonance region where the matching conditions apply, which consists of a strong damping of LWs/EMWs that can also determine the instability saturation. It is, therefore, clear that the effect of H addition in inhomogeneous plasmas requires additional experimental investigation. Theobald *et al.* [25] explored the effects of H on SRS and HE amount in a spherical implosion experiment in which enhanced SRS emission and HE generation were observed for the H-rich target, which was then explained by the occurrence of LDI. In the present experiment, which was conducted under conditions relevant for direct-drive ICF in planer geometry, an increase in both SRS and TPD, and correspondingly in HE generation, was observed when H was present in the ablator. It was found that the variation in plasma inhomogeneity and temperature obtained by H addition was not sufficient to explain the observed results, and the enhancement was therefore mainly attributed to the high IAW damping driven by the H ions into the plasmas, suggesting that LDI caused SRS saturation, whereas other mechanisms such as cavitation and coupling of LWs with IAWs could overwhelm the TPD saturation. These results suggest that a suitable choice of H concentration in the ablator is crucial for mitigating and controlling the SRS, TPD, and HE extent to achieve robust and efficient implosion in direct-drive ICF.

II. EXPERIMENTAL CONDITIONS

A. Laser and target conditions

Experiments were performed at the GEKKO XII-HIPER facility, where a planar target was irradiated with a quasisingle beam [26]. Seven frequency-tripled laser beams (3ω : $\lambda = 351$ nm, $f/15$, $I \sim 2.2 \times 10^{15}$ W/cm²) with a Gaussian temporal profile [full width at half maximum (FWHM) = 230 ps] were combined into an $f/3$ laser bundle delivering an energy of 420–510 J. The spot size was 280 μ m at the FWHM, providing an envelope peak intensity of 1.9×10^{15} to 2.3×10^{15} W/cm². Three frequency-doubled beams (2ω : $\lambda = 527$ nm) were used as the prepulse to produce a preformed scale-length plasma 200 ps before the main pulse. They delivered 250 J in 240 ps with a Gaussian profile and were focused on a spot of 850 μ m FWHM for an intensity of 1×10^{14} W/cm². Examples of pulse shapes of the prepulse for a laser intensity of 1×10^{14} W/cm², the main pulse for a laser intensity of 2×10^{15} W/cm², and the total laser intensity are shown in Fig. 1(a). The 3ω and 2ω beams were mounted on random phase plates (RPPs) and kinoform phase plates, respectively [27,28]. In the experiments, multilayered targets with ablators with and without H (diamond 40 μ m: C; polyethylene 10 μ m: CH₂) were mainly employed, as indicated in Fig. 1(b). A copper layer was employed for the

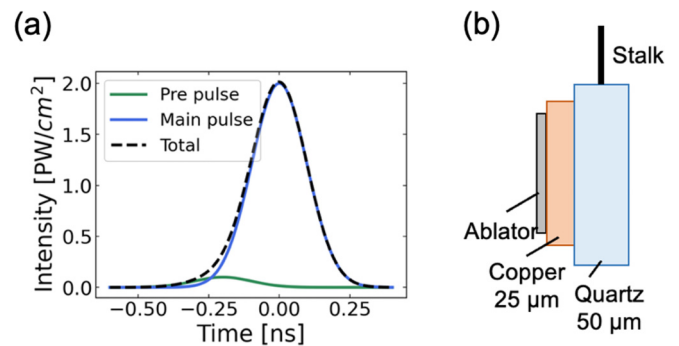


FIG. 1. (a) Examples of laser pulse shapes of the prepulse for a laser intensity of 1×10^{14} W/cm², the main pulse for a laser intensity of 2×10^{15} W/cm², and the total laser intensity. (b) Multilayered target. Diamond: C, and polyethylene: CH₂, were employed as an ablator. A quartz layer was employed for shock measurements, which is not shown in this paper.

absorption of HEs and was used as a marker for HEs via Cu- $K\alpha$ radiation for x-ray diagnostics.

B. Diagnostic conditions

The diagnostic configuration [29] is displayed in Fig. 2. To evaluate SRS and TPD, backscattered light was measured using a time-integrated optical spectrometer (OCEAN Optics, HR2000) and a time-resolved optical spectrometer consisting of a spectrograph and optical streak camera (Hamamatsu, C7700), both located behind the last turning mirrors. The spectral resolutions were 2 and 3 nm, respectively, and the sweep time window of the streak camera was 1.62 or 5.26 ns, leading to a time resolution of 20 or 50 ps. The chromatic time difference in an optical fiber was corrected by considering different reflective indexes based on the Malitson equation in fused quartz [30]. Absolute calibration of the light intensity measured by the time-integrated spectrometer was performed through cross-correlation with the backscattered energy measured by a calorimeter [29,31]. For the HE evaluation, bremsstrahlung continuum x-ray emission with energies >10 keV and Cu- $K\alpha$ x-ray emission (8.048 keV) were measured using a high-energy x-ray spectrometer (HEXS) [32–34] and an x-ray spectrometer, respectively. The HEXS consisted of a stack of image plate (IP; Fujifilm, BAS-MS) layers [35] separated by metallic filters with increasing Z, ranging from Al to Pb [32]. In the analysis, the experimental dose value on each IP was compared with the value given by Monte Carlo simulations of HE propagation into the target using PHITS code [36] to determine their temperature. The x-ray spectrometer consisted of a highly

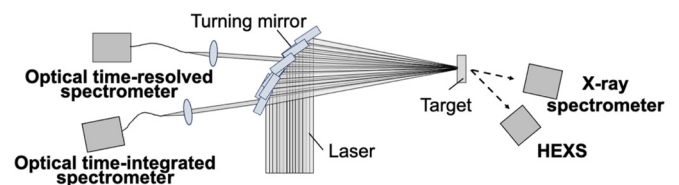


FIG. 2. Schematic of experimental configuration of measuring instruments.

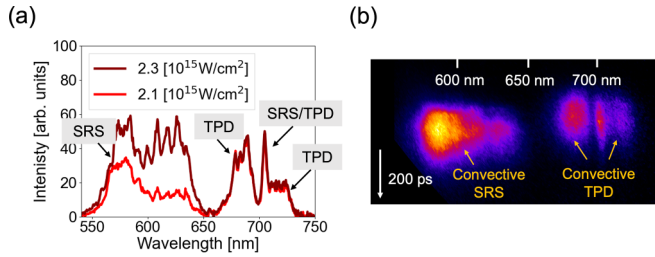


FIG. 3. (a) Backscattered lights from time-integrated optical spectrometer for CH_2 in increasing laser intensity. (b) Typical backscattered light from time-resolved optical spectrometer for CH_2 .

oriented pyrolytic graphite crystal and an IP (Fujifilm, BAS-SR) arranged to detect a spectral range from 7.4 to 8.4 keV including the $\text{Cu-K}\alpha$ line.

III. CHARACTERIZATION OF SRS, TPD, AND HES

In this section, the typical experimental results and their analysis, mainly obtained for the CH_2 targets, are displayed to show the typical characterization of SRS, TPD, and HE generation.

A. Characterization of SRS and TPD

1. Experimental results

Figure 3(a) indicates the time-integrated backscattered spectra in the CH_2 targets measured for two different laser intensities ($I = 2.1 \times 10^{15}$ and $2.3 \times 10^{15} \text{ W/cm}^2$). The observed multippeak spectrum has been described in previous studies [37–39]. A broadband emission $<650 \text{ nm}$ was generated by convective SRS. Near 702 nm, typical half-harmonic ($\omega_0/2$) spectra were observed, where the blue- and redshifted broad peaks were attributed to convective TPD [37,40], whereas the sharp redshifted peak was a signature of hybrid absolute TPD/SRS [37]. When the laser intensity slightly increased by $\sim 10\%$, the spectrally integrated SRS light intensity ($\lambda = 560\text{--}640 \text{ nm}$) increased by a factor of 2.3, corresponding to a rise in reflectivity from $R = 0.03 \pm 0.01\%$ to $0.05 \pm 0.02\%$, respectively, whereas that of TPD ($\lambda = 650\text{--}700 \text{ nm}$) remained virtually the same. Figure 3(b) displays the result of the time-resolved backscattered spectrum measured for a laser intensity of $2.1 \times 10^{15} \text{ W/cm}^2$ as a representative after correcting the chromatic time difference in an optical fiber. The onset time of TPD was 60 ps earlier than that of SRS, which indicates a lower TPD threshold than that of SRS. Note that all shots in the experiment indicated an earlier onset of TPD, with an average of 50 ps.

2. Discussion

One-dimensional radiation-hydrodynamic simulations (ILESTA-1D) [41–43] were performed for each laser and target condition to estimate the plasma conditions, such as electron temperature and plasma density scale length. The electron temperature at $0.25n_c$ (n_c : critical density for $\lambda = 351 \text{ nm}$) was also evaluated from a redshifted sharp peak at $\sim 702 \text{ nm}$ using the formula $\delta\omega/\omega_0 = 2.2 \times 10^{-3} T_e$ [37]. Data from the time-resolved optical spectrometer were used for the evaluation. Figure 4 shows the evaluated peak electron temperature and the corresponding simulation results

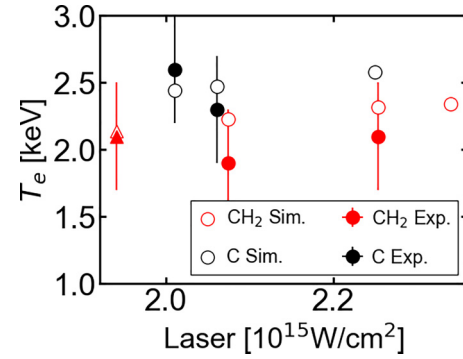


FIG. 4. Plasma temperature from experiment and simulation.

at $0.25n_c$ in all shots in the experiment. Note that the triangle plot refers to the results for a shot on a polystyrene (CH) target. The results obtained for the CH and CH_2 targets were similar. Although two shots failed to obtain time-resolved optical spectrometer data owing to technical issues during the experiments, the plasma temperatures evaluated from the experimental data generally demonstrated acceptable agreement with the simulation results within their error bars, verifying the simulation. The electron temperature in a C plasma was higher than that in CH_2 plasmas because of significant collisional absorption. The results of the C targets are discussed in detail in Sec. IV. By using electron temperature at peak laser timing from simulation calculations for a CH_2 target in a laser intensity of $I = 2.1 \times 10^{15} \text{ W/cm}^2$ ($T_e \sim 2.1 \text{ keV}$), density n_e , and parameter $k\lambda_D$ (k : LW wave number, λ_D : Debye length) for convective SRS responsible for emissions in the range of 560–640 nm were calculated from the matching conditions of energy and momentum, obtaining $n_e = 0.11\text{--}0.19 n_c$ and $k\lambda_D = 0.28\text{--}0.19$. The value of $k\lambda_D$ is typically considered a marker for assessing the significance of Landau damping. Here, the employed electron temperatures are comparable throughout the density region for convective SRS based on the ILESTA simulation. For convective TPD, peak emission at 690 nm corresponded to $n_e = 0.23n_c$ and $k\lambda_D = 0.19$, assuming that the instability was driven along the maximum growth rate hyperbola in the wave-vector space. Relying on plasma parameters: $T_e \sim 2.1 \text{ keV}$ and density scale length $L_n = n/(dn/dt) \sim 65 \mu\text{m}$, the envelope laser intensity was less than the threshold of convective SRS ($\sim 1.5 \times 10^{16} \text{ W/cm}^2$) [44] yet greater than that of convective TPD ($\sim 1.2 \times 10^{15} \text{ W/cm}^2$) [44]. This suggests that convective SRS occurred only in local higher-intensity regions produced by RPP speckles [31,45], by the superposition among the beams, and by the subsequent self-focusing [46], indicating that SRS was far from the saturation regime, which agrees with the steep rise in SRS with laser intensity, as described in the section above. In fact, by considering the probability distribution of local intensity among the speckles $P(I)$ [47], it can be estimated that high-intensity speckles exceeding the threshold of convective SRS (i.e., $I > 7I_0$, where I_0 is the envelope beam intensity, which was $\sim 2.2 \times 10^{15} \text{ W/cm}^2$) comprised $\sim 10\%$ of the total laser energy from $\int_7^\infty IP(I)dI / \int_0^\infty IP(I)dI$. Here, the distribution function of the local intensities was calculated from $P(I) = -dM/dI$, where $M(I) \propto$

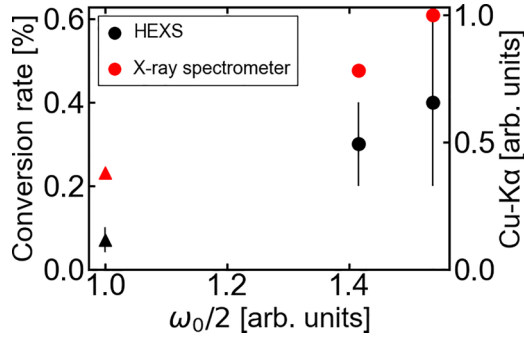


FIG. 5. Conversion rate from high-energy x-ray spectrometer (HEXS) analysis and Cu- $K\alpha$ intensity from x-ray spectrometer. The left axis shows the HEXS results (the conversion rate), and the right axis shows the x-ray spectrometer results (Cu- $K\alpha$ intensity).

$[(I/I_0)^{3/2} - (\frac{3}{10})(I/I_0)^{1/2}] \exp[-(I/I_0)]$ is the abundance of local maxima of the intensity above level I_0 (envelope peak intensity of a single beam) [47]. Therefore, $IP(I)$ is the power-weighted speckle probability. Here, $P(I)$ was negative at $<2I_0$; therefore, we defined $P(I) = 0$ for $I < 2I_0$. [48]. However, convective TPD is expected to occur in the saturation regime as the $\omega_0/2$ intensity remains virtually the same with increasing laser intensity. This is further confirmed by the comparison with previous experiments conducted at the OMEGA laser [49], indicating that TPD saturates when the parameter $IL_n/T_e > 350$ [10^{14} Wmm/cm² keV]; in the present experiment, these parameters were in the range of 570–700. Note that the results obtained for SRS and TPD, including the timing, are consistent with a previous study that referred to an experiment conducted in GEKKO-XII under similar experimental conditions [31].

B. Characterization of HEs

The HEXS data analysis enabled the estimation of the temperature and energy conversion efficiency of HEs, obtaining 25 keV and 0.3%, respectively, in the CH₂ target for a laser intensity of 2.1×10^{15} W/cm². Because the reflectivity of convective SRS was 0.03% in the shot, i.e., considerably less than the HE conversion efficiency, SRS only marginally contributed to the generation of HEs, which was, therefore, mainly produced by TPD. The conversion efficiency of the laser energy to HE calculated from the HEXS data and the values of the Cu- $K\alpha$ integrated intensity measured using the x-ray spectrometer are plotted in Fig. 5 as a function of the integrated light intensity at $\omega_0/2$ ($\lambda = 650$ – 700 nm) for CH and CH₂ targets. The triangle plots refer to the CH target, and the date of one shot is missing from Fig. 5 because it did not contain a Cu layer for the x-ray measurements. Both the values of the conversion rate and those of the Cu- $K\alpha$ intensity are consistent and correlate with $\omega_0/2$ light intensities owing to TPD.

IV. H EFFECTS

In this section, we demonstrate and discuss a comparison of the experimental results obtained with C and CH₂ targets, providing direct evidence of the effects of H in the ablator.

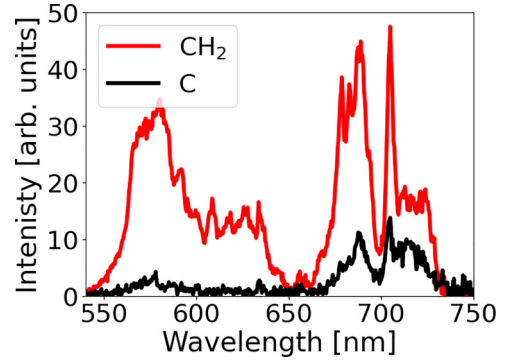


FIG. 6. Backscattered lights from time-integrated optical spectrometer for C and CH₂.

A. Experimental results

Figure 6 shows the time-integrated backscattered spectra measured for two shots (C and CH₂ target) under the same laser conditions (main pulse: $I = 2.1 \times 10^{15}$ W/cm² and prepulse: $I = 1.0 \times 10^{14}$ W/cm²). The shapes of the spectra are similar, indicating broad peak emissions at ~ 580 nm emitted by convective SRS ($n_e \sim 0.13n_c$) and at ~ 690 nm due to convective TPD ($n_e \sim 0.23n_c$). However, the spectrally integrated intensity of SRS light ($\lambda = 560$ – 640 nm) for the shot on the CH₂ target was 14 times greater than that obtained on the C target, whereas the ratio of the integrated intensities of $\omega_0/2$ ($\lambda = 650$ – 700 nm) was reduced to five. Correspondingly, the Cu- $K\alpha$ intensity from the x-ray spectrometer suggests that the HE fluence in the CH₂ target was four times greater than that in the C target. Here, different HE stopping and x-ray radiation powers in different ablator materials were corrected using PHITS simulation, where C (3.5 g/cm³ 40 μ m) and CH₂ (0.96 g/cm³ 10 μ m) with a 25 μ m Cu layer were employed as targets. In the simulations, an electron beam at a temperature of 25 keV in the Maxwellian distribution was injected from the normal direction into the target, and the Cu- $K\alpha$ fluence was tracked behind the Cu layer. In this approach, we evaluated the relative conversion rate of HE into Cu- $K\alpha$ intensity by a factor of 7.4. Thus, the experimental ratio of the Cu- $K\alpha$ raw data intensity between C and CH₂ targets, equal to 27, was reduced to four to represent an actual ratio of HE. Again, the increase in HEs can be explained by enhanced TPD. Here, the HEXS signals in the C targets were overly low to allow a reliable analysis to compare the results of the CH₂ target presented above.

B. Discussion

1. Rosenbluth gain factor

The possible mechanisms responsible for the different enhancements in SRS and TPD are discussed. The Rosenbluth gain factors [50] for convective SRS and TPD (G_{SRS} and G_{TPD}) were calculated based on the plasma parameters provided by the hydrosimulations. They describe the exponential enhancement of an initial plasma modulation produced by instability growth in inhomogeneous plasmas and are depicted as $G = 2\pi\gamma_0^2/\kappa'|v_1v_2|$, where γ_0 , κ' , and $v_{1,2}$ are the homogeneous growth rate, gradient of wave number mismatch,

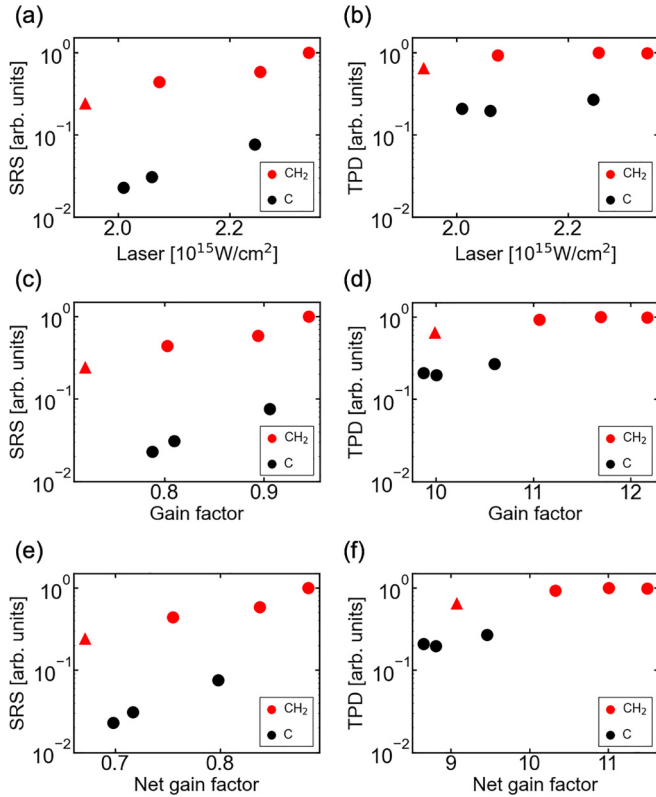


FIG. 7. (a) Relationship between stimulated Raman scattering (SRS) and laser intensity. (b) Relationship between two-plasmon decay (TPD) and laser intensity. (c) Relationship between SRS and gain factor. (d) Relationship between TPD and gain factor. (e) Relationship between SRS and net gain factor. (f) Relationship between TPD and net gain factor. Note that the triangle plots refer to the CH target results.

and group velocity of daughter waves, respectively; it can be easily demonstrated that $G_{\text{SRS}} \propto IL_n$ and $G_{\text{TPD}} \propto IL_n / T_e$ [44]. We obtained G_{SRS} of ~ 0.80 for both C and CH_2 targets at $0.13n_c$ at the peak laser time. Here, G_{TPD} was 10.0 and 11.1 for C and CH_2 , respectively, at $0.23n_c$ at 50 ps before peak laser time. Overall, because $G = 2\pi$ is typically taken as the threshold of instability, SRS was significantly below the threshold, whereas TPD was above the threshold, as mentioned in Sec. III. It should be noted that the electron temperature at $0.13 - 0.23n_c$ was greater for the C plasma than for the CH_2 plasma owing to the higher collisional absorption (e.g., $T_{eC} = 2.5$ keV, $T_{e\text{CH}_2} = 2.2$ keV at peak laser time), as shown in Fig. 4, although the density scale length was virtually the same. This led to a reduced TPD gain in the C plasma compared with that in the CH_2 plasma. Figure 7 displays the plots of spectrally integrated intensity (a) for SRS and (b) for TPD vs laser intensity in all the data shots; Figs. 7(c) and 7(d) display the intensities vs the corresponding Rosenbluth gain factors. Note that the error bars of the plots are within 10%, smaller than the marker size, and the triangle plot refers to the result of a shot on a CH target. The results obtained for the CH and CH_2 targets were similar, which is discussed later in terms of the IAW damping. In TPD, a reasonable decrease in the gain factors for C can be observed. However, as mentioned in

Sec. III, TPD was in a saturated regime, where its growth was only smoothly influenced by the difference in the expected gain, indicating a clear discrepancy in the saturation level between C and CH_2 . Therefore, the different extents of SRS and TPD between the C and CH_2 targets cannot be explained in terms of the Rosenbluth gain factors.

2. Effects of collisional and Landau damping

Damping of daughter waves reduces the growth of SRS and TPD to different extents for C and CH_2 plasmas, which could explain the experimental results. Williams *et al.* [51] derived that the net gain factor of convective instability, accounting for the damping of the daughter waves, can be expressed by $GF(\Gamma)$, where the reduction factor $F(\Gamma) = 2[\arccos(\Gamma) - \Gamma\sqrt{1 - \Gamma^2}] / \pi$, $\Gamma = \sqrt{\gamma_1\gamma_2} / \gamma_0$, and $\gamma_{1,2}$ depicts the damping rate of the daughter waves. The damping rates of the EMW and LW were evaluated by considering collisions and the Landau effect as $\gamma_s = (v_{ei} / 2)(\omega_p^2 / \omega_s^2)$ and $\gamma_{\text{LW}} = v_{ei} / 2 + v_{ld}$, where ω_p and ω_s are the plasma and EMW frequencies, respectively, and v_{ei} and v_{ld} are collisional and Landau damping rates, respectively [10]. Figures 7(e) and 7(f) display plots of the SRS and TPD integrated intensities vs the corresponding net gain values. As expected, the gain values became smaller than those obtained in the Rosenbluth gain, as indicated in Figs. 7(c) and 7(d). However, the relative decrease in the net gains for the C and CH_2 targets remained overly small to explain the discrepancy observed in the SRS and $\omega_0/2$ intensities.

3. H effects in SRS

The above results suggest that additional mechanisms influenced by the presence of H in the ablator could have a role in determining the effective growth/saturation of both SRS and TPD. LDI is a possible saturation mechanism for SRS [21–24,52–56]. In addition, kinetic effects such as phase shift, bowing, and self-focusing of LWs due to particle trapping have been suggested to cause SRS saturation [57–60]. Because such kinetic effects do not directly involve ion motion, we evaluated the effect of LDI as a possible cause of the different extents of SRS. In addition, the $k\lambda_{De}$ values of the convective SRS in this experiment ($k\lambda_D = 0.28 - 0.19$) indicate that such kinetic effects were not dominant because kinetic effects in convective SRS are typically observed in higher values of $k\lambda_{De} > 0.3$ [61,62]. The LDI threshold is described in terms of the density fluctuation $(\delta n / n_e)_{\text{LDI}} = 4k\lambda_{De}\sqrt{(v_{\text{IAW}}/\omega_{\text{IAW}})(v_{\text{LW}}/\omega_{\text{LW}})}$, where k , λ_{De} , v , and ω are the LW wave number, Debye length, damping rate, and frequency, respectively [63]. As demonstrated by this expression, a high IAW damping rate leads to a high LDI threshold, which results in favorable conditions for SRS because excitation of LDI significantly reduces the instability growth, leading to a lower reflectivity level [54,55,64]. Here, IAW damping rates were calculated at a plasma density of $0.13n_c$ from the plasma dielectric function: i.e., $1 + \chi_e + \sum_{\beta} \chi_{i\beta} = 0$, where χ_e and $\chi_{i\beta}$ denote the susceptibility of electrons and ions β [65], obtaining $v_{\text{IAW}}/\omega_{\text{IAW}} = 0.007$ for C and 0.23 for CH_2 for a laser intensity of 2.1×10^{15} W/cm². It was also confirmed that different ion and electron temperatures attributed to H addition have negligible effects on the IAW damping rate

compared with those of the H ions. The LDI thresholds in terms of density fluctuation were calculated to be 0.006 and 0.022, respectively, reasonably verifying a lower reflectivity level of SRS in the C plasma with respect to the CH₂ plasma. It should also be noted that the v_{IAW}/ω_{IAW} ratio for the CH plasma was 0.26; the difference with respect to CH₂ plasma was only 10%, explaining the similar SRS intensities obtained for CH and CH₂ targets [51].

4. H effects in TPD

LDI is also a possible saturation mechanism in TPD [66,67]. However, a much smaller discrepancy of measured $\omega_0/2$ intensity for C and CH₂ plasma compared with that of SRS implies that other saturation mechanisms overwhelmed in the case of TPD. This is in agreement with previous simulation works, suggesting that TPD is saturated by ion density fluctuation and cavitation [40,68,69]. Weber and Riconda [70] demonstrated the transition from LDI-induced saturation occurring at a low plasma temperature of ~ 0.5 keV to saturation by cavity and density fluctuation in plasmas at a temperature of 2 keV and greater, like our case. In terms of IAW damping, Myatt *et al.* [71] demonstrated that the HE flux from TPD doubled with a 20 times increase in the IAW damping rate owing to a favorable nucleation-collapse-burnout cycle in cavitation, which was comparable with our results (four times enhanced HE by 30 times increased IAW damping). In addition, Seaton and Arber [72] suggested the same tendency in terms of the coupling of LWs by IAW (i.e., ion density fluctuation). Our results are a clear experimental indication of the dependence of TPD on the IAW damping rate. However, because the relative weight of each mechanism depends on different interaction parameters, a detailed discussion of TPD saturation in our experimental conditions requires dedicated particle-in-cell-code calculations in the future.

V. SUMMARY

In summary, we experimentally explored the effects of H in the ablator on laser plasma instabilities in direct-drive ICF conditions, observing a clear enhancement of SRS, TPD, and the corresponding HE amount when H is present in the target. The data analysis suggested that the main cause of enhancement was the high IAW damping in plasmas containing H, depicting a scenario where LDI was the main saturation mechanism for convective SRS, whereas a different mechanism, such as cavitation and coupling of LWs by IAW, could be dominant in the saturation of convective TPD. The sensitivity of the IAW damping rate to H concentration was significant. For example, a nanocrystalline diamond containing an H concentration of 4 at. % [73] doubles the IAW damping rate compared with a pure carbon ablator in direct-drive conditions. These results suggest that a suitable choice of H concentration and even tuning the H concentration in the ablator material are crucial for the success of direct-drive ICF.

All experimental data were saved in the SEDNA system at the Institute of Laser Engineering, Osaka University. The data supporting the findings of this study are available from the corresponding author upon reasonable request.

ACKNOWLEDGMENTS

The authors would like to thank the dedicated technical support of the staff at the Institute of Laser Engineering for the laser operation, target fabrication, and plasma diagnostics. This paper was conducted with support and under the auspices of the NIFS Collaboration Research Program (No. 2021NIFS21KUGK136). This paper was also supported by the Japan Society for Promotion of Science, KAKENHI Grant No. JP22J22774, and partially supported by a grant from the MEXT Quantum Leap Flagship Program No. JPMXS0118067246.

-
- [1] J. Nuckolls, L. Wood, A. Thiessen, and G. Zimmerman, Laser compression of matter to super-high densities: Thermonuclear (CTR) applications pressure: Implosion, ablation, *Nature (London)* **239**, 139 (1972).
 - [2] J. Lindl, Development of the indirect-drive approach to inertial confinement fusion and the target physics basis for ignition and gain, *Phys. Plasmas* **2**, 3933 (1995).
 - [3] R. S. Craxton, K. S. Anderson, T. R. Boehly, V. N. Goncharov, D. R. Harding, J. P. Knauer, R. L. McCrory, P. W. McKenty, D. D. Meyerhofer, J. F. Myatt *et al.*, Direct-drive inertial confinement fusion: A review, *Phys. Plasmas* **22**, 110501 (2015).
 - [4] V. A. Smalyuk, D. Shvarts, R. Betti, J. A. Delettrez, D. H. Edgell, V. Yu. Glebov, V. N. Goncharov, R. L. McCrory, D. D. Meyerhofer, P. B. Radha *et al.*, Role of Hot-Electron Preheating in the Compression of Direct-Drive Imploding Targets with Cryogenic D₂ Ablators, *Phys. Rev. Lett.* **100**, 185005 (2008).
 - [5] R. Betti, C. D. Zhou, K. S. Anderson, L. J. Perkins, W. Theobald, and A. A. Solodov, Shock Ignition of Thermonuclear Fuel with High Areal Density, *Phys. Rev. Lett.* **98**, 155001 (2007).
 - [6] S. Gus'kov, X. Ribeyre, M. Touati, J. L. Feugeas, P. Nicolaï, and V. Tikhonchuk, Ablation Pressure Driven by an Energetic Electron Beam in a Dense Plasma, *Phys. Rev. Lett.* **109**, 255004 (2012).
 - [7] R. Nora, W. Theobald, R. Betti, F. J. Marshall, D. T. Michel, W. Seka, B. Yaakobi, M. Lafon, C. Stoeckl, J. Delettrez *et al.*, Gigabar Spherical Shock Generation on the OMEGA Laser, *Phys. Rev. Lett.* **114**, 045001 (2015).
 - [8] K. Kawasaki, Y. Hironaka, Y. Maeda, T. Iwasaki, D. Tanaka, K. Miyanishi, H. Nagatomo, S. Fujioka, N. Ozaki, R. Kodama *et al.*, The role of hot electrons on ultrahigh pressure generation relevant to shock ignition conditions, *High Energy Density Phys.* **37**, 100892 (2020).
 - [9] S. Atzeni and J. Meyer-ter-Vehn, *The Physics of Inertial Fusion* (Oxford University Press, Oxford, 2004).
 - [10] W. L. Kruer, *The Physics Of Laser Plasma Interactions* (CRC Press, Boca Raton, 2019).
 - [11] R. M. Stevenson, L. J. Suter, K. Oades, W. Kruer, G. E. Slark, K. B. Fournier, N. Meezan, R. Kauffman, M. Miller, S. Glenzer *et al.*, Effects of plasma composition on backscatter, hot

- electron production, and propagation in underdense plasmas, *Phys. Plasmas* **11**, 2709 (2004).
- [12] R. K. Follett, J. A. Delettrez, D. H. Edgell, V. N. Goncharov, R. J. Henchen, J. Katz, D. T. Michel, J. F. Myatt, J. Shaw, A. A. Solodov *et al.*, Two-Plasmon Decay Mitigation in Direct-Drive Inertial-Confinement-Fusion Experiments Using Multilayer Targets, *Phys. Rev. Lett.* **116**, 155002 (2016).
- [13] J. R. Fein, J. P. Holloway, M. R. Trantham, P. A. Keiter, D. H. Edgell, D. H. Froula, D. Haberberger, Y. Frank, M. Fraenkel, E. Raicher *et al.*, Mitigation of hot electrons from laser-plasma instabilities in high-z, highly ionized plasmas, *Phys. Plasmas* **24**, 032707 (2017).
- [14] J. Biener, D. D. Ho, C. Wild, E. Woerner, M. M. Biener, B. S. El-dasher, D. G. Hicks, J. H. Eggert, P. M. Celliers, G. W. Collins *et al.*, Diamond spheres for inertial confinement fusion, *Nucl. Fusion* **49**, 112001 (2009).
- [15] Sh. Michaelson, O. TERNYAK, R. Akhvediani, O. A. Williams, D. Gruen, and A. Hoffman, Hydrogen concentration and bonding in nano-diamond films of varying grain sizes grown by different chemical vapor deposition methods, *Phys. Status Solidi* **204**, 2860 (2007).
- [16] K. Kawasaki, D. Tanaka, H. Yamada, S. Ohmagari, Y. Mokuno, A. Chayahara, T. Tamagawa, Y. Hironaka, K. Yamanoi, M. Tsukamoto *et al.*, Direct-drive implosion experiment of diamond capsules fabricated with hot filament chemical vapor deposition technique, *Phys. Plasmas* **28**, 104501 (2021).
- [17] K. Kawasaki, H. Yamada, H. Nagatomo, Y. Hironaka, K. Yamanoi, D. Tanaka, T. Idesaka, Y. Mokuno, A. Chayahara, T. Shimaoka *et al.*, Fabrication of nanocrystalline diamond capsules by hot-filament chemical vapor deposition for direct-drive inertial confinement fusion experiments, *Diam. Relat. Mater.* **135**, 109896 (2023).
- [18] L. Liu, J. Huang, X. He, T. Wang, Z. He, K. Du, and X. Diao, Preparation and characterization of high quality diamond like carbon films on Si microspheres, *Mater. Lett.* **220**, 309 (2018).
- [19] V. J. Rico, F. Yubero, J. P. Espinós, J. Cotrino, A. R. González-Elipé, D. Garg, and S. Henry, Determination of the hydrogen content in diamond-like carbon and polymeric thin films by reflection electron energy loss spectroscopy, *Diam. Relat. Mater.* **16**, 107 (2007).
- [20] Y. Izawa, T. Norimatsu, and C. Yamanaka, Target fabrication activities in Japan, *J. Vac. Sci. Technol. A* **3**, 1252 (1985).
- [21] J. C. Fernández, J. A. Cobble, B. H. Failor, D. F. DuBois, D. S. Montgomery, H. A. Rose, H. X. Vu, B. H. Wilde, M. D. Wilke, and R. E. Chrien, Observed Dependence of Stimulated Raman Scattering on Ion-Acoustic Damping in Hohlraum Plasmas, *Phys. Rev. Lett.* **77**, 2702 (1996).
- [22] R. K. Kirkwood, B. J. MacGowan, D. S. Montgomery, B. B. Afeyan, W. L. Kruer, J. D. Moody, K. G. Estabrook, C. A. Back, S. H. Glenzer, M. A. Blain *et al.*, Effect of Ion-Wave Damping on Stimulated Raman Scattering in High-Z Laser-Produced Plasmas, *Phys. Rev. Lett.* **77**, 2706 (1996).
- [23] D. S. Montgomery, B. B. Afeyan, J. A. Cobble, J. C. Fernández, M. D. Wilke, S. H. Glenzer, R. K. Kirkwood, B. J. MacGowan, J. D. Moody, E. L. Lindman *et al.*, Evidence of plasma fluctuations and their effect on the growth of stimulated Brillouin and stimulated Raman scattering in laser plasmas, *Phys. Plasmas* **5**, 1973 (1998).
- [24] R. K. Kirkwood, R. L. Berger, C. G. R. Geddes, J. D. Moody, B. J. MacGowan, S. H. Glenzer, K. G. Estabrook, C. Decker, and O. L. Landen, Scaling of saturated stimulated Raman scattering with temperature and intensity in ignition scale plasmas, *Phys. Plasmas* **10**, 2948 (2003).
- [25] W. Theobald, A. Bose, R. Yan, R. Betti, M. Lafon, D. Mangino, A. R. Christopherson, C. Stoeckl, W. Seka, W. Shang *et al.*, Enhanced hot-electron production and strong-shock generation in hydrogen-rich ablators for shock ignition, *Phys. Plasmas* **24**, 120702 (2017).
- [26] C. Yamanaka, Y. Kato, Y. Izawa, K. Yoshida, T. Yamanaka, T. Sasaki, M. Nakatsuka, T. Mochizuki, J. Kuroda, and S. Nakai, Nd-doped phosphate glass laser systems for laser-fusion research, *IEEE J. Quantum Electron.* **17**, 1639 (1981).
- [27] Y. Kato, K. Mima, N. Miyanaga, S. Arinaga, Y. Kitagawa, M. Nakatsuka, and C. Yamanaka, Random Phasing of High-Power Lasers for Uniform Target Acceleration and Plasma-Instability Suppression, *Phys. Rev. Lett.* **53**, 1057 (1984).
- [28] S. N. Dixit, K. A. Nugent, J. K. Lawson, K. R. Manes, and H. T. Powell, Kinoform phase plates for focal plane irradiance profile control, *Opt. Lett.* **19**, 417 (1994).
- [29] T. Tamagawa, Y. Hironaka, K. Kawasaki, D. Tanaka, T. Idesaka, N. Ozaki, R. Kodama, R. Takizawa, S. Fujioka, A. Yogo *et al.*, Development of an experimental platform for the investigation of laser-plasma interaction in conditions relevant to shock ignition regime, *Rev. Sci. Instrum.* **93**, 063505 (2022).
- [30] I. H. Malitson, Interspecimen comparison of the refractive index of fused silica, *J. Opt. Soc. Am.* **55**, 1205 (1965).
- [31] G. Cristoforetti, P. Koester, S. Atzeni, D. Batani, S. Fujioka, Y. Hironaka, S. Hüller, T. Idesaka, K. Katagiri, K. Kawasaki *et al.*, Multibeam laser plasma interaction at Gekko XII laser facility in conditions relevant for direct-drive inertial confinement fusion, *High Power Laser Sci. Eng.* **11**, E24 (2023).
- [32] S. Kojima, M. Hata, N. Iwata, Y. Arikawa, A. Morace, S. Sakata, S. Lee, K. Matsuo, K. F. F. Law, H. Morita *et al.*, Electromagnetic field growth triggering super-ponderomotive electron acceleration during multi-picosecond laser-plasma interaction, *Commun. Phys.* **2**, 99 (2019).
- [33] C. D. Chen, J. A. King, M. H. Key, K. U. Akli, F. N. Beg, H. Chen, R. R. Freeman, A. Link, A. J. Mackinnon, A. G. MacPhee *et al.*, A bremsstrahlung spectrometer using *k*-edge and differential filters with image plate dosimeters, *Rev. Sci. Instrum.* **79**, 10E305 (2008).
- [34] P. Koester, F. Baffigi, G. Cristoforetti, L. Labate, L. A. Gizzi, S. Baton, M. Koenig, A. Colaitis, D. Batani, A. Casner *et al.*, Bremsstrahlung cannon design for shock ignition relevant regime, *Rev. Sci. Instrum.* **92**, 013501 (2021).
- [35] A. L. Meadowcroft, C. D. Bentley, and E. N. Stott, Evaluation of the sensitivity and fading characteristics of an image plate system for x-ray diagnostics, *Rev. Sci. Instrum.* **79**, 113102 (2008).
- [36] T. Sato, Y. Iwamoto, S. Hashimoto, T. Ogawa, T. Furuta, S.-i. Abe, T. Kai, P.-E. Tsai, N. Matsuda, H. Iwase *et al.*, Features of particle and heavy ion transport code system (PHITS) version 3.02, *J. Nucl. Sci. Technol.* **55**, 684 (2018).
- [37] W. Seka, B. B. Afeyan, R. Boni, L. M. Goldman, R. W. Short, K. Tanaka, and T. W. Johnston, Diagnostic value of odd-integer half-harmonic emission from laser-produced plasmas, *Phys. Fluids* **28**, 2570 (1985).
- [38] G. Cristoforetti, L. Antonelli, S. Atzeni, F. Baffigi, F. Barbato, D. Batani, G. Boutoux, A. Colaitis, J. Dostal, R. Dudzak *et al.*, Measurements of parametric instabilities at laser

- intensities relevant to strong shock generation, *Phys. Plasmas* **25**, 012702 (2018).
- [39] G. Cristoforetti, L. Antonelli, D. Mancelli, S. Atzeni, F. Baffigi, F. Barbato, D. Batani, G. Boutoux, F. D'Amato, J. Dostal *et al.*, Time evolution of stimulated Raman scattering and two-plasmon decay at laser intensities relevant for shock ignition in a hot plasma, *High Power Laser Sci. Eng.* **7**, e51 (2019).
- [40] R. Yan, A. V. Maximov, C. Ren, and F. S. Tsung, Growth and Saturation of Convective Modes of the Two-Plasmon Decay Instability in Inertial Confinement Fusion, *Phys. Rev. Lett.* **103**, 175002 (2009).
- [41] H. Takabe, M. Yamanaka, K. Mima, C. Yamanaka, H. Azechi, N. Miyanaga, M. Nakatsuka, T. Jitsuno, T. Norimatsu, M. Takagi *et al.*, Scalings of implosion experiments for high neutron yield, *Phys. Fluids* **31**, 2884 (1988).
- [42] H. Terasaki, T. Sakaiya, K. Shigemori, K. Akimoto, H. Kato, Y. Hironaka, and T. Kondo, *In situ* observation of the Rayleigh-Taylor instability of liquid Fe and Fe-Si alloys under extreme conditions: Implications for planetary core formation, *Matter Radiat. Extrem.* **6**, 054403 (2021).
- [43] T. Sakaiya, H. Takahashi, T. Kondo, T. Kadono, Y. Hironaka, T. Irifune, and K. Shigemori, Sound velocity and density measurements of liquid iron up to 800 GPa: A universal relation between Birch's law coefficients for solid and liquid metals, *Earth Planet. Sci. Lett.* **392**, 80 (2014).
- [44] C. Z. Xiao, Z. J. Liu, C. Y. Zheng, and X. T. He, Competition between stimulated Raman scattering and two-plasmon decay in inhomogeneous plasma, *Phys. Plasmas* **23**, 022704 (2016).
- [45] H. A. Rose and D. F. DuBois, Statistical properties of laser hot spots produced by a random phase plate, *Phys. Fluids B* **5**, 590 (1993).
- [46] D. Pesme, S. H. Iler, J. Myatt, C. Riconda, A. Maximov, V. T. Tikhonchuk, C. Labaune, J. Fuchs, S. Depierreux, and H. A. Baldis, Laser-plasma interaction studies in the context of megajoule lasers for inertial fusion, *Plasma Phys. Control. Fusion* **44**, B53 (2002).
- [47] J. Garnier, Statistics of the hot spots of smoothed beams produced by random phase plates revisited, *Phys. Plasmas* **6**, 1601 (1999).
- [48] D. Turnbull, A. V. Maximov, D. Cao, A. R. Christopherson, D. H. Edgell, R. K. Follett, V. Gopalaswamy, J. P. Knauer, J. P. Palastro, A. Shvydky *et al.*, Impact of spatiotemporal smoothing on the two-plasmon-decay instability, *Phys. Plasmas* **27**, 102710 (2020).
- [49] D. H. Froula, B. Yaakobi, S. X. Hu, P.-Y. Chang, R. S. Craxton, D. H. Edgell, R. Follett, D. T. Michel, J. F. Myatt, W. Seka *et al.*, Saturation of the Two-Plasmon Decay Instability in Long-Scale-Length Plasmas Relevant to Direct-Drive Inertial Confinement Fusion, *Phys. Rev. Lett.* **108**, 165003 (2012).
- [50] M. N. Rosenbluth, Parametric Instabilities in Inhomogeneous Media, *Phys. Rev. Lett.* **29**, 565 (1972).
- [51] E. A. Williams, Convective growth of parametrically unstable modes in inhomogeneous media, *Phys. Fluids B* **3**, 1504 (1991).
- [52] S. Depierreux, C. Labaune, J. Fuchs, D. Pesme, V. T. Tikhonchuk, and H. A. Baldis, Langmuir Decay Instability Cascade in Laser-Plasma Experiments, *Phys. Rev. Lett.* **89**, 045001 (2002).
- [53] D. T. Michel, S. Depierreux, C. Stenz, V. Tassin, and C. Labaune, Exploring the Saturation Levels of Stimulated Raman Scattering in the Absolute Regime, *Phys. Rev. Lett.* **104**, 255001 (2010).
- [54] T. Kolber, W. Rozmus, and V. T. Tikhonchuk, Saturation of stimulated Raman scattering by Langmuir and ion-acoustic wave coupling, *Phys. Fluids B* **5**, 138 (1993).
- [55] C. Labaune, H. A. Baldis, B. S. Bauer, V. T. Tikhonchuk, and G. Laval, Time-resolved measurements of secondary Langmuir waves produced by the Langmuir decay instability in a laser-produced plasma, *Phys. Plasmas* **5**, 234 (1998).
- [56] S. Depierreux, J. Fuchs, C. Labaune, A. Michard, H. A. Baldis, D. Pesme, S. Hüller, and G. Laval, First Observation of Ion Acoustic Waves Produced by the Langmuir Decay Instability, *Phys. Rev. Lett.* **84**, 2869 (2000).
- [57] H. X. Vu, D. F. DuBois, and B. Bezzerides, Transient Enhancement and Detuning of Laser-Driven Parametric Instabilities by Particle Trapping, *Phys. Rev. Lett.* **86**, 4306 (2001).
- [58] L. Yin, W. Daughton, B. J. Albright, B. Bezzerides, D. F. DuBois, J. M. Kindel, and H. X. Vu, Nonlinear development of stimulated Raman scattering from electrostatic modes excited by self-consistent non-Maxwellian velocity distributions, *Phys. Rev. E* **73**, 025401(R) (2006).
- [59] L. Yin, B. J. Albright, K. J. Bowers, W. Daughton, and H. A. Rose, Saturation of Backward Stimulated Scattering of a Laser Beam in the Kinetic Regime, *Phys. Rev. Lett.* **99**, 265004 (2007).
- [60] A. Friou, D. Bénisti, L. Gremillet, E. Lefebvre, O. Morice, E. Siminos, and D. J. Strozzi, Saturation mechanisms of backward stimulated Raman scattering in a one-dimensional geometry, *Phys. Plasmas* **20**, 103103 (2013).
- [61] D. S. Montgomery, J. A. Cobble, J. C. Fernández, R. J. Focia, R. P. Johnson, N. Renard-LeGalloudec, H. A. Rose, and D. A. Russell, Recent trident single hot spot experiments: Evidence for kinetic effects, and observation of Langmuir decay instability cascade, *Phys. Plasmas* **9**, 2311 (2002).
- [62] S. J. Spencer, A. G. Seaton, T. Goffrey, and T. D. Arber, Inflationary stimulated Raman scattering in shock-ignition plasmas, *Phys. Plasmas* **27**, 122705 (2020).
- [63] S. J. Karttunen, Ion fluctuation effects on the two-plasmon decay and stimulated Raman scattering, *Phys. Rev. A* **23**, 2006 (1981).
- [64] R. P. Drake and S. H. Batha, The influence of subsidiary Langmuir decay on the spectrum of stimulated Raman scattering, *Phys. Fluids B* **3**, 2936 (1991).
- [65] Q. S. Feng, C. Y. Zheng, Z. J. Liu, C. Z. Xiao, Q. Wang, and X. T. He, Excitation of nonlinear ion acoustic waves in CH plasmas, *Phys. Plasmas* **23**, 082106 (2016).
- [66] H. X. Vu, D. F. DuBois, D. A. Russell, and J. F. Myatt, The reduced-description particle-in-cell model for the two plasmon decay instability, *Phys. Plasmas* **17**, 072701 (2010).
- [67] R. K. Follett, D. H. Edgell, R. J. Henchen, S. X. Hu, J. Katz, D. T. Michel, J. F. Myatt, J. Shaw, and D. H. Froula, Direct observation of the two-plasmon-decay common plasma wave using ultraviolet Thomson scattering, *Phys. Rev. E* **91**, 031104(R) (2015).
- [68] A. B. Langdon, B. F. Lasinski, and W. L. Kruer, Nonlinear Saturation and Recurrence of the Two-Plasmon Decay Instability, *Phys. Rev. Lett.* **43**, 133 (1979).

- [69] S. Weber, C. Riconda, O. Klimo, A. Héron, and V. T. Tikhonchuk, Fast saturation of the two-plasmon-decay instability for shock-ignition conditions, *Phys. Rev. E* **85**, 016403 (2012).
- [70] S. Weber and C. Riconda, Temperature dependence of parametric instabilities in the context of the shock-ignition approach to inertial confinement fusion, *High Power Laser Sci. Eng.* **3**, e6 (2015).
- [71] J. F. Myatt, H. X. Vu, D. F. DuBois, D. A. Russell, J. Zhang, R. W. Short, and A. V. Maximov, Mitigation of two-plasmon decay in direct-drive inertial confinement fusion through the manipulation of ion-acoustic and Langmuir wave damping, *Phys. Plasmas* **20**, 052705 (2013).
- [72] A. G. Seaton and T. D. Arber, Laser-plasma instabilities in long scale-length plasmas relevant to shock-ignition, *Phys. Plasmas* **27**, 082704 (2020).
- [73] C. Dawodeit, S. O. Kucheyev, S. J. Shin, T. M. Willey, M. Bagge-Hansen, T. Braun, Y. M. Wang, B. S. El-Dasher, N. E. Teslich, M. M. Biener *et al.*, Grain size dependent physical and chemical properties of thick CVD diamond films for high energy density physics experiments, *Diam. Relat. Mater.* **40**, 75 (2013).